Available online at www.sciencedirect.com
SCIENCE DIRECT®
ELSEVIER
Engineering Geology 68 (2003) 123–139
ENGINEERING GEOLOGY
www.elsevier.com/locate/enggeo

Seventeen years of the "La Clapière" landslide evolution analysed from ortho-rectified aerial photographs

B. Casson*, C. Delacourt, D. Baratoux, P. Allemand

Laboratoire Sciences de la Terre, UMR 5570, Université Claude Bernard Lyon-1 et ENS Lyon, Bat. Géode, 2 Rue Raphaël Dubois, 69622 Villeurbanne Cedex, France

Received 2 October 2001; received in revised form 29 April 2002; accepted 14 June 2002

Abstract

We present a new method of digital elevation model (DEM) calculation from aerial photographs and apply this method to the La Clapière landslide in the Mercantour Massif in eastern France. The method uses new techniques of image correlation and of restitution of camera parameters. The calculated DEMs are used to ortho-rectify three aerial photographs acquired between 1983 and 1999. Measurements, made from these ortho-rectified images, show that the average velocity of the landslide was of 1.7 cm/day, with the rate of the headscarp retreat of 4.1 cm/day, and the toe of the landslide advancing at 1.7 cm/day, between 1983 and 1999. Within the landslide, the velocity field is are relatively homogeneous, although their directions are locally heterogeneous. Scree slopes and scarps develop in an heterogeneous way within the landslide. Because the headscarp moves faster than the front of the landslide, material spreads laterally at the scree slopes, and/or is eroded at the front of the landslide by the river, and/or is accumulated within the landslide, on a low slope area located above a competent bar called Iglière bar.

Keywords: Aerial photogrammetry; DEM; Ortho-rectification; Landslide

1. Introduction

In landslide studies, knowledge of surface movements is an essential part for understanding deformation mechanisms. Movement of the Saint-Etienne-de-Tinée landslide "La Clapière" in the French Southern Alps is about 1 cm/day in average (Follacci et al., 1989). This value is derived from ground-based measurements made by tacheometry. Tacheometric measurements are actually realized with laser on point-like targets located within the landslide and, therefore, indicate local values of deformation. Due to spatial and temporal heterogeneities of the deformations, these ground-based measurements are not sufficient to fully describe the spatial velocity field of the landslide and its evolution.

Remote sensing imagery is a very powerful tool for landslide monitoring because it offers a synoptic view of the landslide that can be repeated at different time intervals. Despite their high potential, satellite imagery, such as synthetic aperture radar (SAR) (Fruneau

* Corresponding author. Tel.: +33-4-72-43-27-42; fax: +33-4-72-44-85-93.
E-mail address: berangere.casson@univ-lyon1.fr (B. Casson).

0013-7952/02/$ - see front matter © 2002 Elsevier Science B.V. All rights reserved.
PII: S0013-7952(02)00201-6

and Achache, 1995) or optical satellite imagery, have only been in existence for about 20 years. Moreover, the spatial resolution of optical satellite imagery systems is typically not adequate for landslide studies until the recent improvements in optical systems, such as in the satellite IKONOS.

Aerial photographs are advantageous for landslide studies in France because they have a suitable spatial resolution and have been in existence for more than 50 years (Pothérat, 1994). However, in order to realize quantitative studies with aerial photographs, the geometrical distortions of the images have to be corrected by an ortho-rectification phase. Ortho-rectification methods exist since 1897 (Baltsavias, 1995) (Th. Scheimpflug, who built a zone transformater to rectify photographs). However, until the 1960s, the ortho-rectification used generally optical projections (Hobbie, 1974). The digital photogrammetric systems (DPS), which generate numerically and automatically digital ortho-rectified images, emerged in the 1980s and 1990s (Goepfert, 1984; Powers et al., 1996). However, some of these methods require the participation of the operator. Nevertheless, most of the time, it is impossible for the operator to control and estimate the accuracy and the resolution of all the points of the ortho-rectified images (Blachut and Van Wijk, 1976; Ducher, 1991). Indeed, these methods which are often presented as software do not allow a total control of the digital chain of treatment of the images. Furthermore, most of commercial DEM calculation and ortho-rectification software is not suitable for the accuracy and resolution required for landslides studies. Moreover, such softwares are often too expensive for academic purposes.

In this paper, we describe a new digital and automatic ortho-rectification line that is based on new algorithms of correlation of images and of optimization of acquisition parameters. In order to correct geometrical distortions of initial images with a high accuracy, accurate digital elevation models (DEM) are processed. Our methodology allows to control the resolution and the precision of our DEM and our ortho-rectified images, all over the digital procedure. Furthermore, global positioning system (GPS) control points are used in order to improve the accuracy of DEMs and of ortho-rectified images. This line has been applied to the "La Clapière" landslide using aerial photographs acquired between 1983 and 1999. From these ortho-rectified images, we have determined the velocity fields of the landslide.

2. Ortho-rectification of aerial photographs using a digital elevation model (DEM)

Topography can be deduced from two aerial photographs (called a stereoscopic pair) acquired of the same area from slightly different points of view. Each point of the first image has to be recognized on the second one by correlation techniques (Kraus et al., 1979). Then combination of the shift values between two homologous points (that is to say to image points that represent a same ground point) and acquisition parameters of the cameras give the height of each point (Wolf and Dewitt, 2000).

2.1. Image geometry

For a stereoscopic pair, a reference system on each image and an absolute ground reference system are defined (Fig. 1). The origin of image reference systems is located at the center of the images, which corresponds to the normal projection of the camera on the photograph. The ξ-axis is defined along the line of flight and the η-axis is perpendicular to the ξ-axis. The image coordinates (ξ,η) represent the distance between the image location of a point and the center of the image (referred to as the principal point). The normal projection of the camera of the first image on the ground represents the origin of the absolute reference system. The X-axis is defined along the W–E direction and the Y-axis along the S–N direction. The Z-axis is perpendicular to the plane (X,Y). Image coordinates (ξ,η) are related to ground coordinates (X,Y,Z) by the following equations from Kraus and Waldhäusl (1994):

$$\begin{cases} \xi = \xi_0 - c\dfrac{r_{11}(X-X_0)+r_{21}(Y-Y_0)+r_{31}(Z-Z_0)}{r_{31}(X-X_0)+r_{23}(Y-Y_0)+r_{33}(Z-Z_0)} \\ \eta = \eta_0 - c\dfrac{r_{12}(X-X_0)+r_{22}(Y-Y_0)+r_{32}(Z-Z_0)}{r_{31}(X-X_0)+r_{23}(Y-Y_0)+r_{33}(Z-Z_0)} \end{cases} \quad (1)$$

where ξ_0 and η_0 represent the principal point location, which is offset from the center of the image, due to obliquity between the film and the optic axis (Mikhail et al., 2001); c is the focal length of the camera; X_0, Y_0 and Z_0 are the camera coordinates in the ground

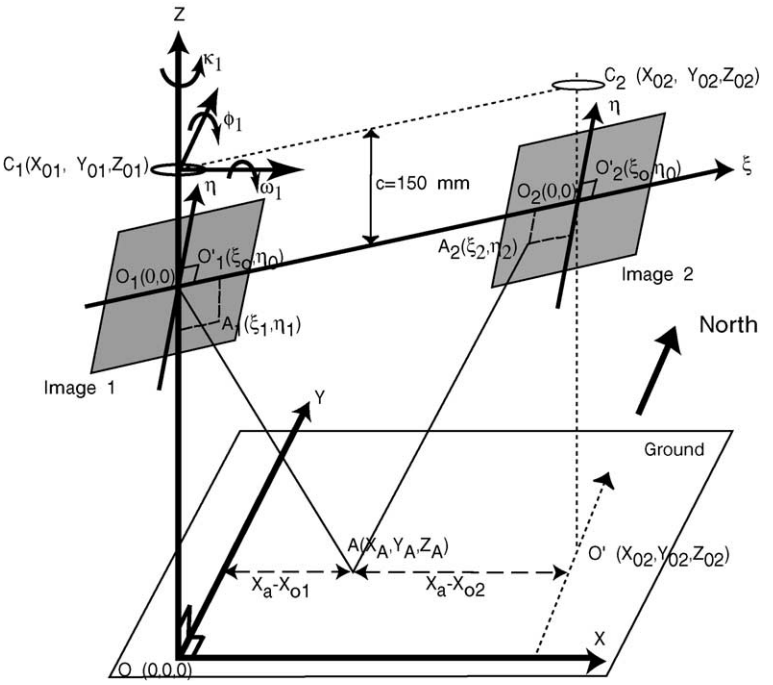

Fig. 1. Reference systems and geometric characteristics of a stereoscopic pair (Kraus et al., 1979; Jensen, 2000), where (X,Y,Z) is the absolute reference system with O as its origin; $C_1(X_{01},Y_{01},Z_{01})$ and $C_2(X_{02},Y_{02},Z_{02})$ are the positions of cameras in the absolute reference system; O' is the vertical projection of the second camera on the ground; ξ, and η are the axes of the image reference systems; $O_1(0,0)$ and $O_2(0,0)$ are the centers of the images; O_1' (ξ_0,η_0) and O_2' (ξ_0,η_0) are the real intersections between optic axis and film which are referred to as the principal points; $A(X_A,Y_A,Z_A)$ $A(X_A,Y_A,Z_A)$ is a ground point and $A_1(\xi_1,\eta_1)$ and $A_2(\xi_2,\eta_2)$ are the corresponding image points; $(X_a\text{-}X_{01})$ is the distance between the A point and the first camera along X-axis; $(X_a\text{-}X_{02})$ is the distance between the A point and the second camera along X-axis; c is the focal length of the camera; $(\kappa_1,\varphi_1,\omega_1)$ are the rotation angles of the first camera.

reference system; and r_{ij} are the members of the rotation matrix R taking into account ω, φ and κ which are the camera rotation angles. The coordinates ξ_0 and η_0 of the principal point and the focal distance c of the acquisition chamber are calculated during the calibration of the acquisition chamber and are included in the header file of the photographs (Pothérat et al., 1999).

Inversely, relations connecting ground coordinates (X,Y,Z) to image coordinates (ξ,η), and given by Kraus and Waldhäusl (1994), are as follows:

$$\begin{cases} X = X_0 + (Z - Z_0)\frac{r_{11}(\xi-\xi_0)+r_{12}(\eta-\eta_0)-r_{13}c}{r_{31}(\xi-\xi_0)+r_{32}(\eta-\eta_0)-r_{33}c} \\ Y = Y_0 + (Z - Z_0)\frac{r_{21}(\xi-\xi_0)+r_{22}(\eta-\eta_0)-r_{23}c}{r_{31}(\xi-\xi_0)+r_{32}(\eta-\eta_0)-r_{33}c} \end{cases} \quad (2)$$

In order to restore topography (i.e. to measure X, Y and Z using image coordinates), two images are required for solving this equation system.

2.2. DEM building

2.2.1. Correlation function

The first step required for building a DEM from two aerial photographs is correlating these images by recognizing identical objects on each image of a stereoscopic pair. Then, each point of the first image has to be associated with the corresponding point on the second image. These pairs of image points, which represent the same ground point, are called homologous points. The recognition and the location of homologous points are numerically obtained by mathematical correlation functions (Kasser and Egels,

2002). The correlation function (p_n) used in our study belongs to the Fourier domain (Schaum and McHugh, 1991). This function is progressively applied to small parts of the two images of the stereoscopic pair, by sliding windows, which cover a same geographic zone, until the entire overlap area has been analyzed. This function shows a correlation peak (Michel and Avouac, 1999) when the homologous points are recognized. The position of the peak, from the center of the correlation window, gives the shift between the homologous points. This shift is used to locate the homologous points on each image, which is essential to calculate the ground position of the point with photogrammetric Eq. (2). Furthermore, the position of the maximum of the peak, and consequently the shift value, is more accurate if the peak is narrow. The formulation (Schaum and McHugh, 1991) of the correlation function in one dimension is:

$$p_n = \frac{1}{N}\sum_{k=0}^{N}\frac{X_k\overline{Y_k}}{\|X_k\overline{Y_k}\|}\exp\left(\frac{2i\pi nk}{N}\right) \quad (3)$$

where X_k is the discreet Fourier transform of the first image and Y_k the discreet Fourier transform of the second one. The normalization of (p_n) by $\|X_k\overline{Y_k}\|$ allows to take into account all frequencies and to obtain a narrow correlation peak.

Relation (3) can be extended to two dimensions in order to correlate images (Schaum and McHugh, 1991). However, due to differences in the acquisition parameters (i.e. angles and positions of the cameras) of a stereoscopic pair, and to local topography, significant distortions between the images occur. These distortions (especially the rotation component) cannot be detected by the correlation function (p_n). When these distortions are present, there is no correlation peak. Therefore, a global correction for both acquisition (Kraus and Waldhäusl, 1994) and topographic distortions (Kasser and Egels, 2002) has to be performed before the correlation phase.

2.2.2. Correction of acquisition distortions

Acquisition distortions for each image are corrected using precise camera positions and angles. Approximate camera positions, acquired by GPS on board, are specified on each photograph. Initial camera angles are considered equal to zero because of the near vertical acquisition (Pothérat et al., 1999). These approximate values have to be improved by a least mean squares minimization. Firstly, ground point

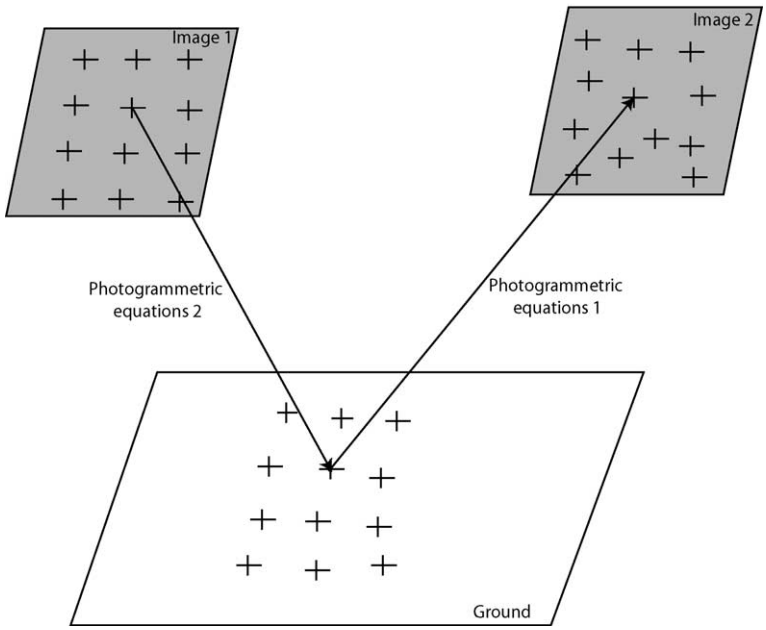

Fig. 2. Principle of the approximate ground location of homologous points after the absolute orientation of the cameras.

localized by GPS are identified on images. Then, photogrammetric Eq. (1) is used to calculate image coordinates of the control points, using initial acquisition parameters and ground positions of the control points. After a first least mean squares minimization, new camera angles and new camera positions are obtained. The convergence is obtained for 15 points equally localized over the whole image. This method is called the absolute orientation of cameras (Kraus and Waldhäusl, 1994).

After the absolute orientation of the cameras, homologous points can be located, without acquisition distortions, on each image of a stereoscopic pair. Firstly, the photogrammetric Eq. (2) is used to locate each point of the first image on a ground plane, situated at the average elevation of control points (Fig. 2). Then Eq. (1) is used to locate each ground point on the second image (Fig. 2). These two steps allow to locate approximately, and without camera distortion, the homologous points on each image of a stereoscopic pair. At this stage of the work, the accuracy of the location of homologous points is still relatively poor but is improved by the correction of topographic distortions and the correlation phase described below.

2.2.3. Correction of distortions due to topography and correlation of homologous points

Two stereoscopic images can be successfully correlated if (1) they overlap the same geographic zone and (2) the geometry of the structures are similar on both images. However, after correction of acquisition distortions, location of a ground point on two images is shifted in the ξ and η directions by the absolute elevation of this point. Indeed, the objects which have to correlate are viewed at different positions and angles, so their projection on two stereoscopic images is different. A direct correlation is then impossible because the rotation between the projections inhibits the correlation function (p_n). The correction of these geometric distortions due to the local topography is necessary. A solution is to find the local slopes of the zone before the DEM calculation (Kasser and Egels, 2002). This step, described below, is used both to determine the local slopes and to correlate the overlap zone of a stereoscopic pair.

After the absolute orientation of the cameras, homologous points are located approximately on each image of a stereoscopic pair. For each pair of homologous points, two windows are extracted, from the stereoscopic images, around the location of the homologous image points. These windows have to overlap in order to be correlated. However, because of

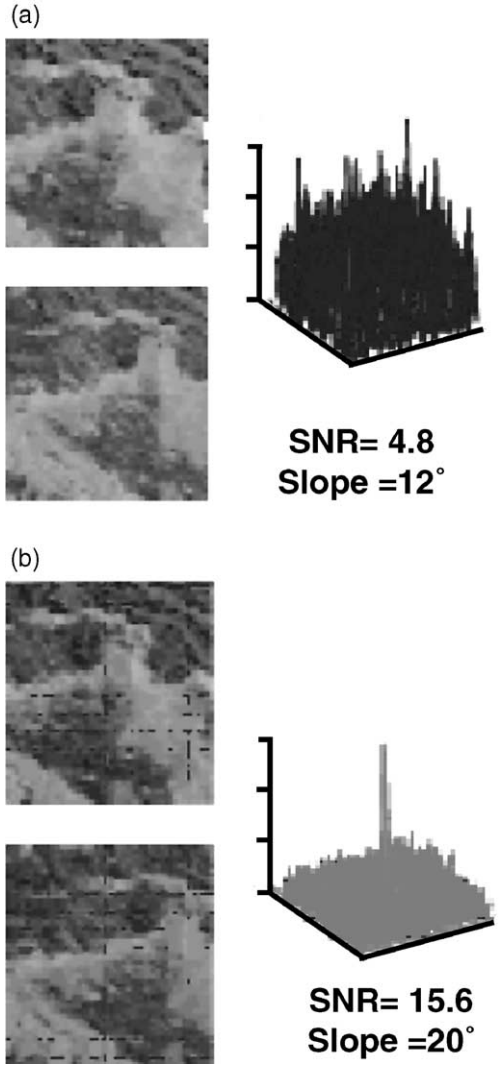

Fig. 3. Example of correlation of two small windows. In the first case (a) windows, associated with a pair of homologous points, are projected on a local slope of 12°. No correlation peak appears, which is confirmed by a low SNR (Signal to Noise Ratio). Consequently, this slope does not represent the real slope of the zone covered by the windows. In the second case (b) the windows are projected to the slope of 20° and present a correlation peak and high SNR result, indicating that this slope represents the real slope of the zone covered by the windows.

the geometric distortions described above, these windows do not correlate directly. They are then projected on an inclined plane which represents the local topography around the studied point (Kasser and Egels, 2002). Slopes between $-40°$ and $+40°$ (which are geologically realistic) are studied with a step of 5° for each pair of windows (Fig. 3). Each pair of windows is projected along each slope. Then the projected windows are correlated with the function (p_n). The slope, which generates the best correlation, is selected as the local slope of the zone covered by the windows (Fig. 3). The criteria for selection of the best correlation is the signal-to-noise ratio (SNR):

$$\mathrm{SNR} = \frac{\max(p_n)}{\mathrm{mean}(p_n)} \tag{4}$$

where $\max(p_n)$ is the maximum of the correlation function (3) and mean (p_n) its average value.

At the end of this step of topographic corrections, a slope map is available which is used to calculate the DEM. The local slopes are firstly estimated for one point over 10,000 with an accuracy of 5°. However, an accurate DEM can not be directly computed using this unrefined slope map. The slopes are then interpolated, from the previous unrefined slope map, over all the points of the overlap area of stereoscopic images. Finally, all homologous points of this overlap area can be correlated with high accuracy. At the end of the correlation phase, all homologous points in the overlapping region are positioned.

2.3. Topography restoration

2.3.1. Relative orientation of the cameras

From Eq. (2) and camera parameters, ground position of two homologous points can be calculated. As the camera parameters are still imprecise for each

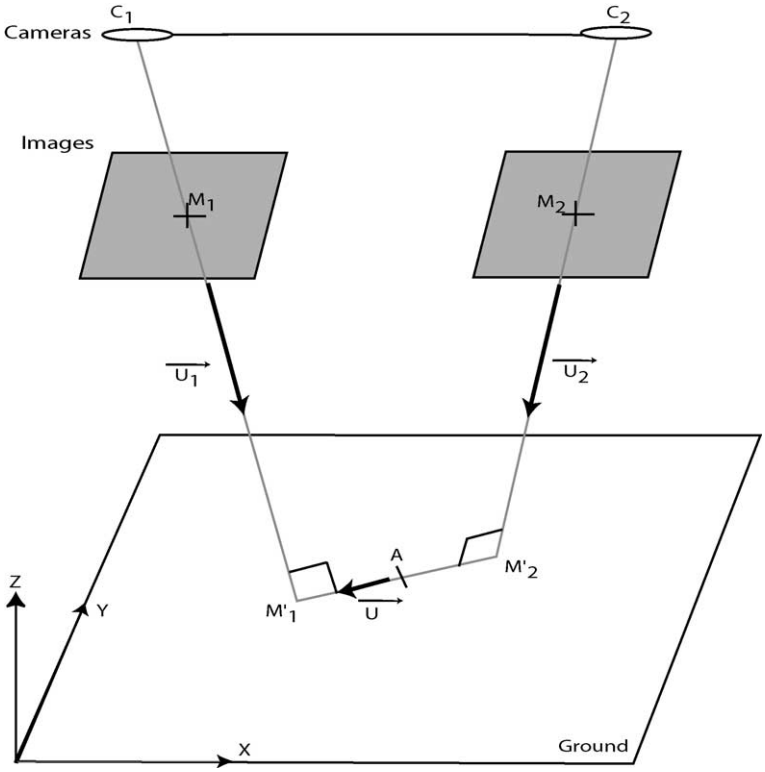

Fig. 4. Vector relations used to build the initial DEM, where X, Y and Z are axes of the ground reference system; O is the origin of the system; C_1 and C_2 are the camera positions; M_1 and M_2 are two homologous points; M_1' and M_2' are the ground points associated with the pair of homologous points $\overrightarrow{u_1}$, $\overrightarrow{u}$ and $\overrightarrow{u_2}$ and are the unit vectors of [C_1M_1'], [$M_2'M_1'$] and [C_2M_2']; A is the middle of the segment [$M_1'M_2'$].

image, two distinct ground positions separated by some tenth of meters are obtained. In ideal conditions, the lines of sight of each camera should intersect on the ground and the distance between the two ground points should tend towards zero. The intersection of the lines of sight is used to constrain the parameters of one camera relative to the other one (Kraus and Waldhäusl, 1994; Baratoux et al., 2001). The parameters of one camera and the *X*-position of the other one are fixed and equal to values calculated during the absolute orientation of cameras. To further improve the homologous points location, the *Y*- and *Z*-positions and the angles of the second camera need to be refined using a least mean square minimization. The best correlated points (about 150 in order to constrain the minimization very well) with the highest SNR are selected. The variable camera parameters are then improved, using results from a least mean square method, which minimizes the differences between the observed coordinates of the best correlated points and their calculated coordinates. At the end of this relative orientation step of the second camera relative to the first one, new angles and new *Y*- and *Z*-positions of the second camera are available. A pair of homologous points always corresponds to two ground points but, after this relative orientation, the distance between the two ground positions of the homologous points is less than to 1 m.

2.3.2. DEM processing

The final acquisition parameters and photogrammetric Eq. (2) is used to build an initial digital elevation model (DEM). In this initial DEM, each ground point corresponds to the center (A) of the segment [M_1' M_2'] where M_1' and M_2' represent the ground positions associated to the homologous image points M_1 and M_2 (Fig. 4). The geometric relation (Appendix A) used to calculate the ground position of A is:

$$\overrightarrow{OA} = \frac{\overrightarrow{OM_1'} + \overrightarrow{OM_2'}}{2} \Leftrightarrow \overrightarrow{OA} = \frac{\overrightarrow{OC_1} + \overrightarrow{OC_2}}{2} + \frac{k_1\overrightarrow{u_1} + k_2\overrightarrow{u_2}}{2} \quad (5)$$

where O is the origin of the ground reference system; C_1 and C_2 are the camera positions; M_1' and M_2' are the ground positions of the pair of homologous points (M_1,M_2); $\overrightarrow{u_1}$ and $\overrightarrow{u_2}$ are the unit vectors of the segments

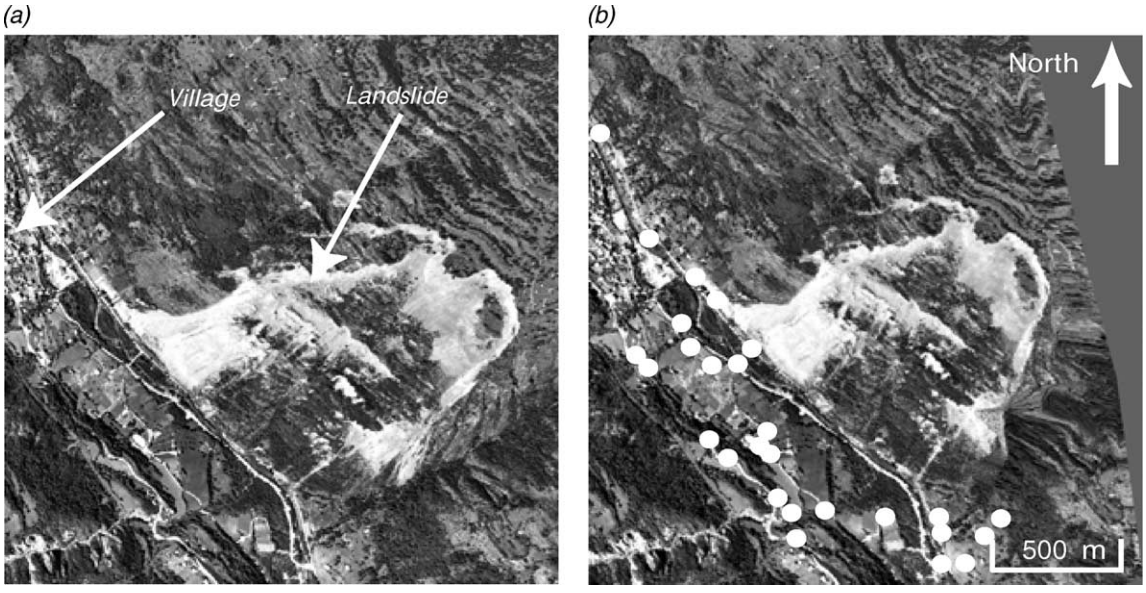

Fig. 5. Example of ortho-rectification of image 60 of mission FP 3540-3840 (above Saint-Etienne-De-Tinée (France) in 1991). (a) Image 60 in acquisition geometry before ortho-rectification—the scale and the north direction are not represented on this photograph because it has no sense on an image in acquisition geometry. (b) Image 60 in cartographic geometry after ortho-rectification with the scale and the north direction—the control points used for the absolute orientation of DEMs are figured (in white) on this image.

$[C_1M_1']$ and $[C_2M_2']$; and k_1 and k_2 are the vectorial coefficients associated with $\overrightarrow{u_1}$ and $\overrightarrow{u_2}$.

The precision of this initial DEM can be improved using a least mean squares method. The least mean squares method determines the corrections necessary (on the variables X, Y, Z) to minimize the differences between the observed and the calculated image location of each DEM point.

2.3.3. DEM absolute orientation

The advantage of the relative orientation procedure is that it produces a very accurate DEM in a non-georeferenced space. The main disadvantage of this method is that the DEM coordinates have been modified from the absolute space. This modification is a geometric transformation consisting of a translation T, a rotation R and a scaling multiplier m as (Baratoux et al., 2001):

$$[XYZ_{GPS}] = T + mR[XYZ_{DEM}] \quad (6)$$

where $[XYZ_{GPS}]$ are ground coordinates of a point measured by GPS and $[XYZ_{DEM}]$ are the DEM coordinates of the same point.

The parameters T, R and m are estimated by a least mean squares method using GPS ground coordinates of control points and the DEM coordinates of the same control points. The minimization of the differences between the observed ground positions of control points (GPS coordinates) and their calculated

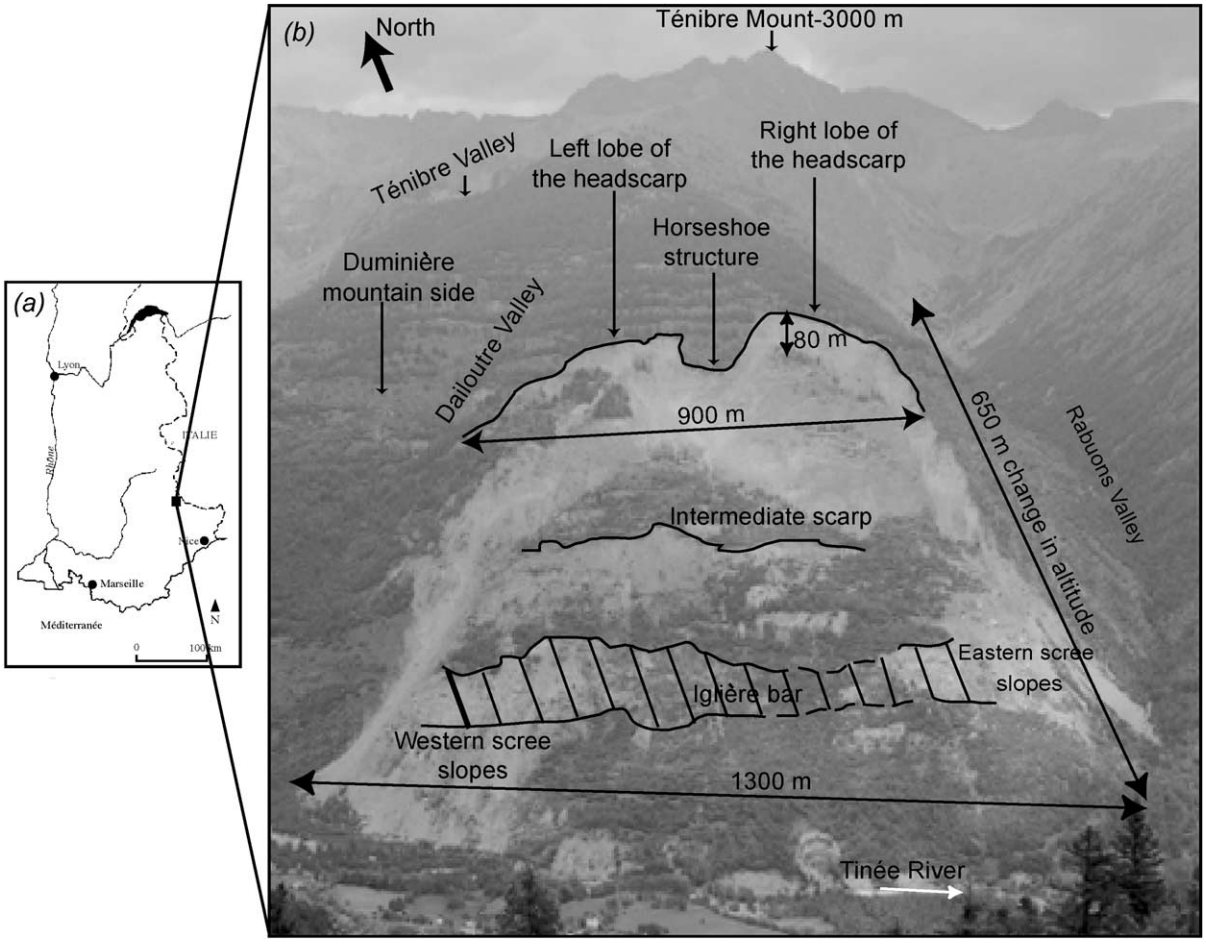

Fig. 6. (a) Geographic location of the La Clapière landslide (44°15′ 20.0N–6°56′ 37.7E). (b) Major geomorphologic characteristics of La Clapière landslide.

positions (DEM coordinates) is used to calculate the corrections which must be applied to an initial set *T*, *R* and *m* parameters. For the first iteration of minimization, *T* and *R* are set equal to zero and the *m* parameter is set to 1. At the end of the minimization, *T*, *R* and *m* parameters are known and the DEM is oriented to the map reference system.

The absolute DEM is then used to ortho-rectify the images (i.e. to project each image point of an aerial photograph into a map geometry (Fig. 5). Indeed, the ground positions *X*, *Y* and *Z* (given by DEM) of each point and the acquisition parameters are used in the photogrammetric relations (2) in order to calculate the coordinates ξ and η of each point on the ortho-rectified image.

3. "La Clapière" evolution

3.1. Geology and history of "La Clapière" landslide

The "La Clapière" landslide is in the Mercantour massif (France), on the left bank of the Tinée River, downstream from the village of Saint-Etienne-de-Tinée (Fig. 6). The landslide represents a major human and economic hazard because of its active scree slopes and the possibility of the formation and collapse of a landslide dam, which could flood both upstream and downstream areas (Follaci, 1987). The lateral extent of the landslide is about 1.3 km between the northwestern Dailoutre valley and the southeastern Rabuons valley. The vertical extent of the landslide is about 650 m (between 1100 and 1750 m height). The volume of the landslide is about 50 Mm^3 (Follaci, 1987). The headscarp of the landslide is marked by a rocky outcrop (Fig. 6b) that has two lobes joined by a horseshoe structure. Another scarp occurs at the middle of the landslide. A third scarp is located just below a competent and continuous layer of stratified metadiorites called the Iglière bar. Two scree slopes are developed below this third escarpment: one on the east just above the Rabuons valley and one on the west above the river (Fig. 6b; Pothérat, 1994). The slope of the landslide reaches 40° below the Iglière bar but is always less than 25° above the Iglière bar. Two lithologic units have been identified in the region of the landslide (Malaroda, 1970; Follaci, 1987; Fig. 7). A lower Triassic to Upper Cretaceous sedimentary unit, partially overlain by recent fluvial and glacial sediments, crops out on the (southwest) bank of the river. On the (northeast) bank of the river, the landslide deforms Annelle metamorphic and migmatitic basement rock, principally composed of plagioclasic and lenticular-banded gneiss. The Iglière bar represents a subhorizontal and mechanical discontinuity in the gneiss unit near the altitude of 1300 m. All units are foliated (strike N130°E, dip 0–10°SW) and few zones present mylonitic structures (Fabbri and Cappa, 2001; Gunzburger and Laumonier, 2002). The massif also contains numerous fractures (Follacci et al., 1988; Pothérat, 1994), which are favorable for rainfall

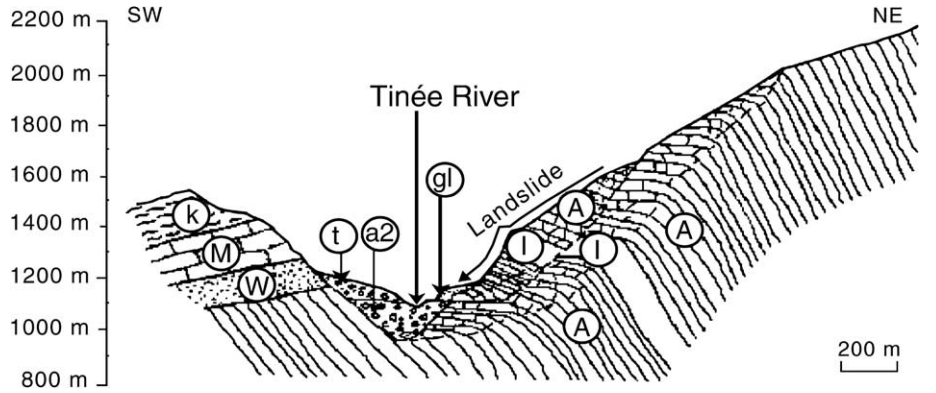

Fig. 7. Geologic section through the landslide (from Follaci, 1987). Quaternary units: t = torrential ejecta; gl = fluvial and glacial deposits; a2 = alluvium. Sedimentary units: k = gypsum marls; M = Triassic limestone; W = Werfenian sandstone. Metamorphic units: A = migmatitic gneiss of Annelle; I = metadiorite of Iglière.

infiltration which in turn can affect landslide movement (Julian and Anthony, 1996).

The first indication of landslide movement was noticed about 1900. First aerial photographs showing the landslide were acquired in 1955. In 1985, the road closest to the landslide was closed because of dangerous scree slopes. A second road, built on the south bank of the river, was closed in 1986 (Pothérat, 1994; Fruneau, 1995). Between 1982 and 1986, landslide movement was always less than 2 cm/day (Follaci, 1999). However, between 1986 and 1988 the velocity of the landslide was greater than 10 cm/day. In 1988, a tunnel was built to divert the river so that the landslide would not dam the flow if it filed catastrophically (Fruneau, 1995). Since 1988, the activity of the landslide has decreased, although the movements have always been more than 1 cm/day. Greater than average rainfall in 1997 caused short-term increases in landslide movement (Follaci, 1999).

3.2. Data set

Three aerial stereoscopic photographs acquired in 1983, 1991 and 1999 by the French Geographical Institute (IGN) have been used in this study (Table 1, Fig. 8). Images were acquired vertically at a constant elevation of about 5 km. Each image covers about 36 km^2. As the time between two acquisitions does not exceed 1 min, more than 60% of overlap is realised between the individual images of stereoscopic pairs (Pothérat et al., 1999). The images were initially acquired on film. Then they were scanned by the IGN on a photogrammetric scanner. Using the three stereoscopic pairs of 1983, 1991 and 1999 (Table 1), three DEMs have been processed following the methodology described in the first part of this paper.

Table 1
References and characteristics of images and accuracy of DEMs

	1983	1991	1999
Images references			
Images references	787–788	60–61	434–435
Mission reference	IFN 06P	FP 3540–3840	FD06
Images and camera characteristics			
Surface of the covered area (km^2)	15.28	47,61	33.06
Images scale	1:17,000	1:30,000	1:25,000
Focal distance (mm)	213.81	151.792	152.754
Principal point, ξ_0	0.006	−0.013	−0.005
Positions (mm), η_0	−0.006	0.005	−0.001
Relative accuracy of DEM (m)	2.3	3.17	3.02
Absolute accuracy of DEM (m)	6.3	7.2	6.2

The resolution and accuracy of measurements obtained from these photographs are directly dependent on the DEM resolution and accuracy. In our case, the DEM's resolution is equal to scanned image resolution of 1.27 m (Table 1). Consequently, the best resolution of ortho-rectified images is 1.27 m. Accuracy maps (Fig. 8), deduced from residuals of the least mean squares minimization used to build the relative DEMs (cf. Section 2.3.2) indicate that accuracy in landslide region is less than 3 m (Fig. 8). Nevertheless, the absolute accuracy of the DEMs, estimated from residuals of the minimization of the DEMs absolute orientation (cf. Section 2.3.3), is about 7 m (Table 1). Consequently, the accuracy of differential measurements on ortho-rectified images correspond to the cumulated absolute accuracy of each DEM that is about 20 m.

3.3. Motion analysis

3.3.1. Variation of landslide dimensions

The total surface of the landslide was about 1.3 km^2 in 1983 and increased by about 12% between 1983 and 1999 (Fig. 9a). The total length of the landslide increased in 130 ± 20 m on the west side and 370 ± 20 m on the east side (Fig. 9c). This lengthening occurred by a 110 ± 20 m frontal advancement on the west side of the landslide while the western lobe of the headscarp was nearly stable (Fig. 10). On the east, this lengthening was due to both a 110 ± 20 m frontal advancement and a 260 ± 20 m retreat of the eastern lobe of the headscarp (Fig. 10). The width of the landslide was 1040 ± 20 m at the top and 1450 ± 20 m at the bottom in 1983 (Fig. 9d). The width of the landslide remained stable at the top between 1983 and 1999 and increased at the bottom by 62 ± 20 m to the west during the same period (Fig. 9d). This basal width variation is attributed to an expansion of scree slopes at the toe of the landslide.

3.3.2. Evolution of scarps and scree slopes

The surface of scree slopes doubled between 1983 and 1991 (Fig. 9a) and covered about 60% of the

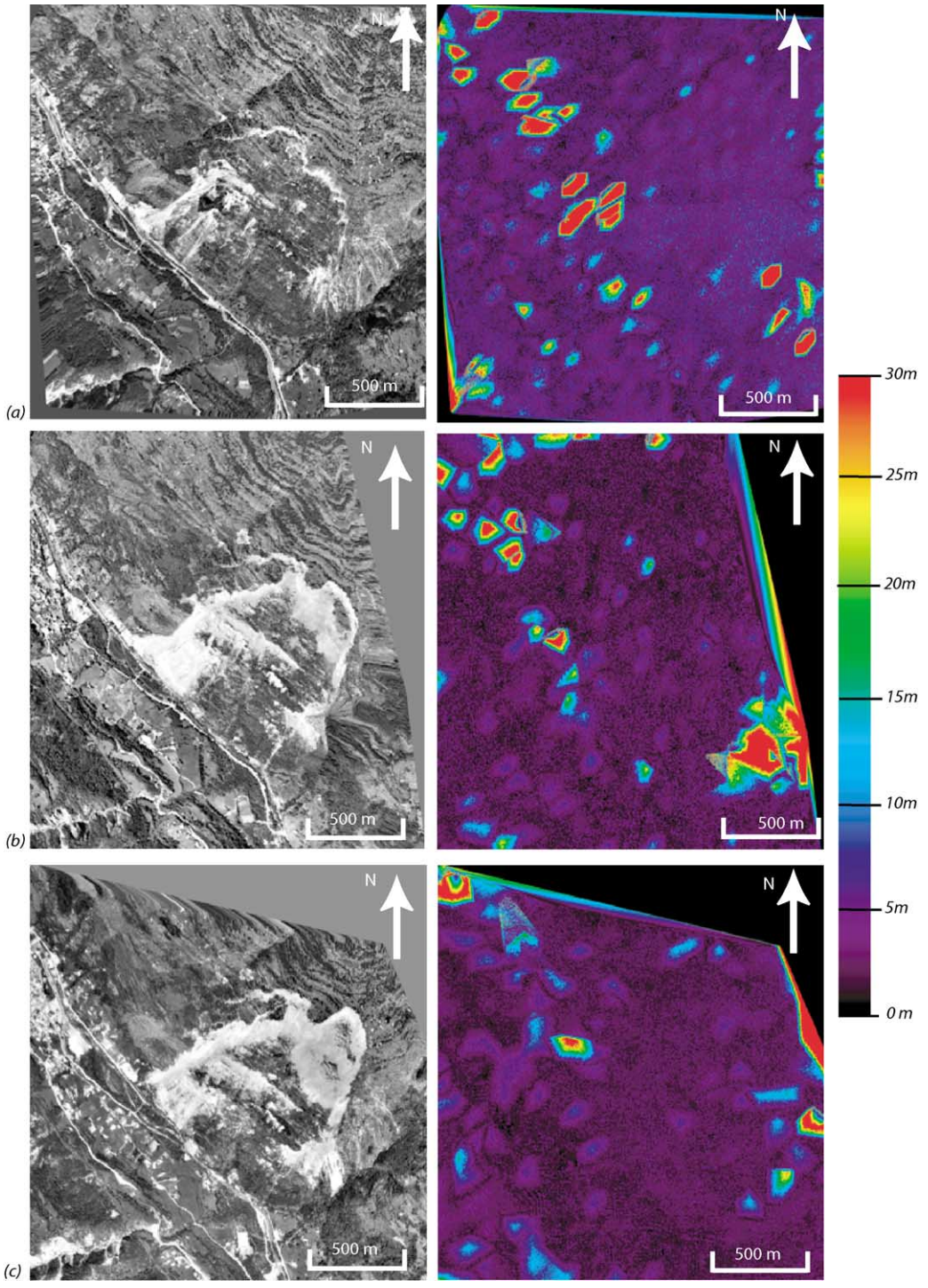

Fig. 8. Ortho-rectified images used to study the landslide evolution. They are presented with the accuracy map of each DEM which points out the high precision of the landslide region. (a) Image of 1983 and its accuracy map. (b) Image of 1991 and its accuracy map. (c) Image of 1999 and its accuracy map.

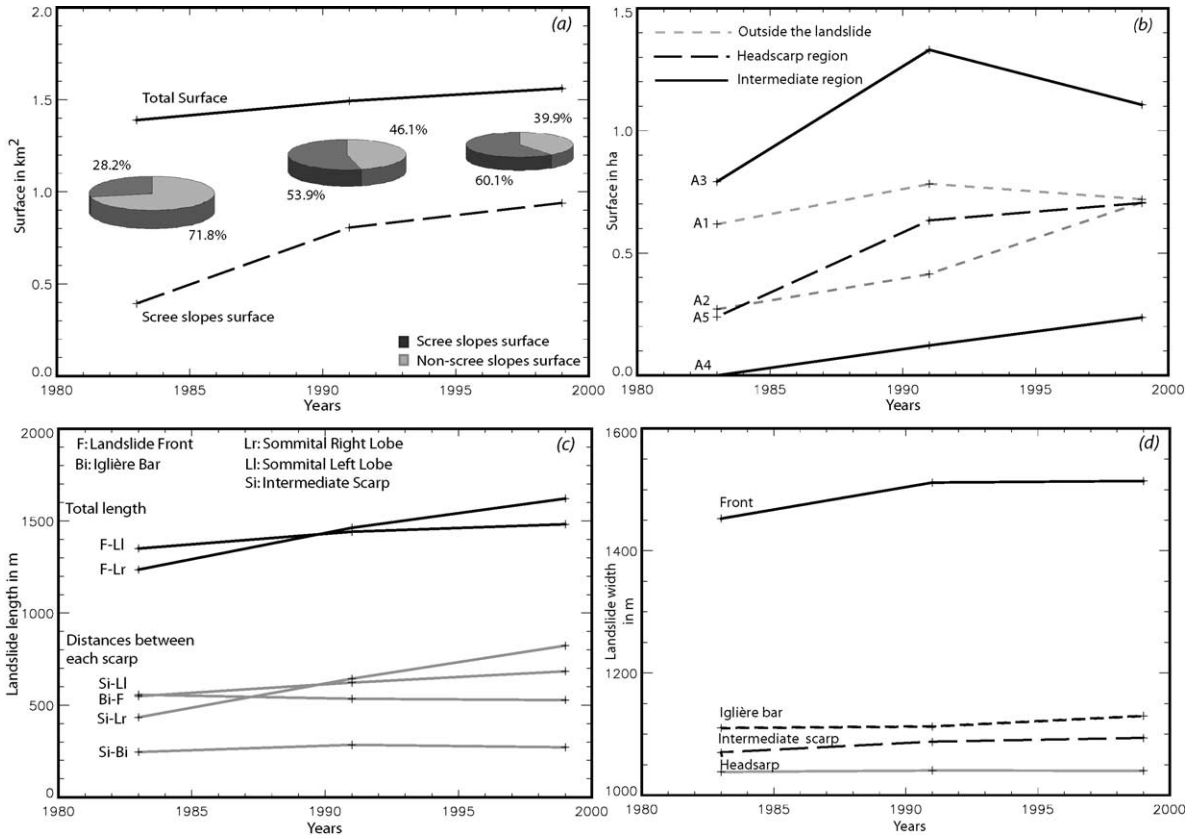

Fig. 9. Graphs showing evolution of the dimensions of the landslide. (a) Evolution of surface areas. (b) Evolution of scree slopes areas—location of A1–A5 are shown in Fig. 10. (c) Length of geomorphic features. (d) Width of geomorphic features.

landslide in 1999. Since 1983, new scree slopes have developed on the west side of the landslide. The surface of two of these scree slopes (*A*1 and *A*2—Figs. 9b and 10) increased of 16% (*A*1) and 159% (*A*2) between 1983 and 1999. Field inspections show that opening of fissures takes place in these areas (Gunzburger, 2001). The fissures indicate that the landslide is expanding to the west into an area that is just above the village of Saint-Etienne-de-Tinée. On the east, the fault of the Rabuons valley strictly bounds the landslide. On the west, the fault of the Dailoutre valley does not bound the landslide, which could extend beyond it, probably up to the Ténibre valley (Fig. 6).

The horseshoe structure at the head of the landslide, already in place in 1983, moved 60 ± 20 m downslope between 1983 and 1991. Since this date, this structure is stable. Two lobes separated by the horseshoe structure show a distinct evolution with the right lobe being more active than the left one (Figs. 9c and 10). The right lobe was especially active between 1983 and 1991. Moreover, surface of scree slopes below this scarp increased. For example, the surface of scree slopes *A*3 increased by 40% and a new scree slopes *A*4 appeared and developed at the same time (Fig. 9b). However, between 1991 and 1999, the vegetation has reconquered the surface of *A*3 slopes, indicating a decrease in movements in this area. Nevertheless, the area of scree slopes *A*4 and the headscarp retreat increased in the same time (Figs. 9b,c and 10). These observations indicate the displacement of active zones within the landslide. The asymmetry between the right and the left lobes of the headscarp is attributed to the fault with an azimuth N45E in the middle of the landslide (Fig. 1).

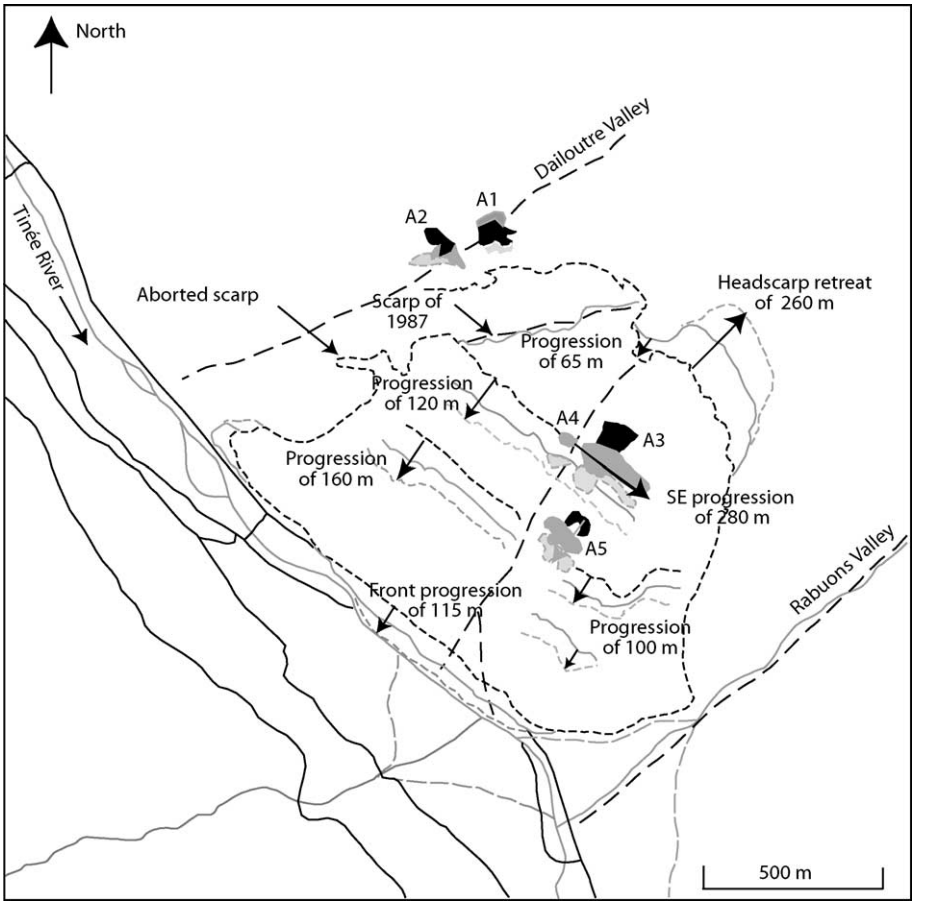

Fig. 10. Landslide evolution. (⋯) Landslide boundaries and scarp surfaces in 1983. (▬) Landslide boundaries and scarp surfaces in 1991. (▬) Landslide boundaries and scarp surfaces in 1999. (▬ ▬) Major faults. (▬ ▬) Alluvial fans. (▬) Rivers. (▬) Roads.

In 1987 (Follaci, 1987), a new scarp appeared below the western headscarp (Fig. 10). It is associated with scree slopes expansion just below the scarp. These scree slopes result from the disaggregation of surface material under the effect of the surface fracturing and are not associated with movements within the landslide.

The intermediate scarp grew laterally by 280 ± 20 m to the east and 110 ± 20 m downslope between 1983 and 1991 (Fig. 10). New scree slopes developed east of this intermediate scarp. Between 1991 and 1999, these scree slopes have reached 0.45 ha in surface. Furthermore, an aborted scar on the western side of the landslide did not show any movement between 1983 and 1999.

The basal scarp (Fig. 10), which occurs below the Iglière bar, did not record any lateral growth, but a 154 ± 20 m downslope advancement on the west and a 110 ± 20 m downslope advancement on the east. The difference between the eastern and the western parts of the landslide is indicative of large variations in the evolution of scarps and scree slopes, which can be perhaps related to the presence of fault.

3.3.3. Internal movements and mass conservation

Internal movements were measured on 14 characteristic points which are easily visible on each orthorectified photograph. The average displacement of all the points is about 104 ± 20 m between 1983 and

1999 (Fig. 11a,b,c). The velocities were uniform at about 1.7 cm/day between 1983 and 1991 and between 1991 and 1999. Similarly the displacements of the intermediate and basal scarps and their frontal advancement were 1.7 cm/day (Fig. 10d), indicating an homogeneous velocity field throughout the landslide. The velocities greater than 1 cm/day in average are in good agreement with the tacheometric data (Follaci, 1999) acquired on the landslide since 1979. This validates our method of DEM and ortho-rectification processing.

When analyzed in detail, the velocity field is homogeneous in term of intensity and quite heterogeneous in term of direction. Indeed, if the general direction of the displacement vectors is along the dip line of the landslide, the vectors located just below

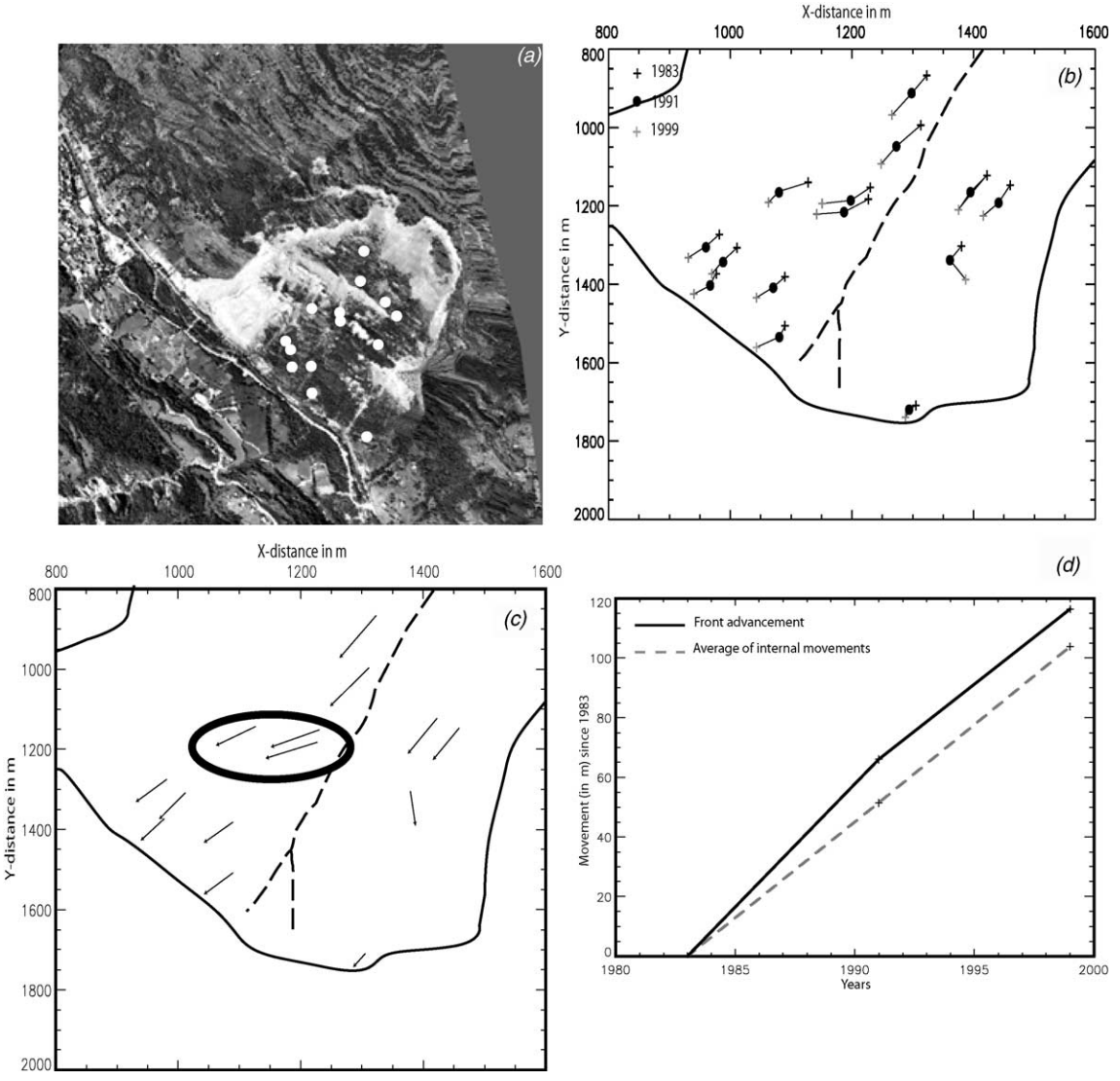

Fig. 11. Graphs showing the internal movements within the landslide. (a) Location of internal points (in white). (b) Displacement of internal points between 1983 and 1991 and between 1991 and 1999. (c) Displacement vectors of internal points between 1983 and 1999. (d) Frontal advancement and average of internal points.

the Iglière bar present a different direction. In this area, the direction of the displacement is more lateral, at over 45° angle with respect to the main part of the landslide (Fig. 11c). Follaci (1987) suggested that the Iglière bar, which did not record any movement before 1987, and began to advance downslope that year.

The record of internal movements, frontal advancement and scarp enlargement are then used to estimate the mass conservation within the landslide. The length between the intermediate scarp and the Iglière bar and the length between the Iglière bar and the front remained constant between 1983 and 1999 (Fig. 10). In the same time the intermediate, the basal scarp and the front progressed about 100 m downslope, and the same observation is valid for the internal points (Fig. 11d). This demonstrates that the entire area between the intermediate scarp and the front was translated downslope. Assuming that the thickness of the landslide is constant over this area, we deduce that frontal erosion or accumulation due to this translation is very weak. However, the landslide was also affected, by about 260 m a headscarp retreat, at a velocity of 4.1 cm/day (Fig. 9c). Then, the material destabilized by the retreat could have firstly been evacuated by erosion by the river at the front of the landslide or/and been accumulated at toe of the landslide. Secondly, this material could have spread laterally, which is in agreement with the wide shape of the landslide, the basal extent of the scree slopes and the dynamics of scree zones. Material could have been accumulated in the landslide, suggesting that La Clapière became thicker. One possible zone of accumulation is above the Iglière bar, where the slope values are lower than in the rest of the landslide. Further studies, such as differential DEM analysis are necessary to verify this hypothesis.

4. Conclusions

A new methodology for DEM derivation from stereoscopic aerial photographs has been developed. This methodology benefits from new techniques of image correlation and improvement of restitution of camera parameters by automatic least mean squares minimization techniques. DEMs are used to ortho-rectify aerial images acquired at different periods. Furthermore, a map showing the accuracy for each point of the DEM, and consequently for each point of ortho-rectified images, is provided with each DEM. This method of DEM processing, applied on three aerial photographs of the "La Clapière" landslide acquired between 1983 and 1999, allowed for a quantitative and accurate assessment of the different parts of the landslide and their evolution through time. The average velocity measured on the ortho-rectified images of the landslide was 1.7 cm/day during this period. The velocity of headscarp retreat (4.1 cm/day) was faster than the frontal advancement velocity (1.7 cm/day). Furthermore, the frontal advancement velocity was the same as the average internal motion (1.7 cm/day). The ortho-rectified photographs reveal that the landslide is expanding to the west which may pose a threat to the Saint-village of Etienne-de-Tinée in the future. The dynamics of scree slopes and scarps appear to be different between the eastern and the western part of the landslide, probably due to the influence of the fault in the middle of the landslide. Despite the limited temporal sampling of this study (8 years), the method is well suited for the long-term study of landslides. This long-term study is of great importance to an understanding of the evolution of landslides. The method could be integrated with differential SAR interferometry technique which can supply deformation data over different time periods.

Acknowledgements

This work has been financially supported by the company Image, the CNES (Centre National des études spatiales), ACI 'Prevention des catastrophes naturelles' and PNTS French INSU programs, and EEC-RETINA project.

Appendix A. Initial DEM building

Geometric relations (Fig. 4) are used to restore topography. The following vector relation is used to link image and ground positions of each pair of homologous points:

$$\overrightarrow{C_1C_2} = \overrightarrow{C_1M_1'} + \overrightarrow{M_1'M_2'} + \overrightarrow{M_2'C_2} \quad (7)$$

The unit vectors $\overrightarrow{u_1}$ and $\overrightarrow{u_2}$ of the segments $[C_1M_1']$ and $[M_2'\ C_2]$ are defined as

$$\overrightarrow{u_1} = \frac{\overrightarrow{C_1M_1'}}{\|\overrightarrow{C_1M_1'}\|} \quad \overrightarrow{u_2} = \frac{\overrightarrow{C_2M_2'}}{\|\overrightarrow{C_2M_2'}\|} \tag{8}$$

The segment $[M_1'\ M_2']$, perpendicular to $[C_1M_1']$ and $[M_2'\ C_2]$, represents the smallest length between the segments $[C_1M_1']$ and $[M_2'\ C_2]$. So this unit vector is calculated using the vectorial product:

$$\overrightarrow{u} = \overrightarrow{u_1} \wedge \overrightarrow{u_2} \tag{9}$$

Then, using relations (8) and (9), Eq. (7) becomes:

$$\overrightarrow{C_1C_2} = k_1\overrightarrow{u_1} - k\overrightarrow{u} - k_2\overrightarrow{u_2} \tag{10}$$

where k_1, k_2 and k are the unknown vectorial coefficients.

The matrix form of Eq. (10) is:

$$\begin{pmatrix} C_1C_{2x} \\ C_1C_{2y} \\ C_1C_{2z} \end{pmatrix} = \begin{pmatrix} u_{x1} & -u_x & -u_{x2} \\ u_{y1} & -u_y & -u_{y2} \\ u_{z1} & -u_z & -u_{z2} \end{pmatrix} \begin{pmatrix} k_1 \\ k \\ k_2 \end{pmatrix} \tag{11}$$

where C_1C_{2x}, C_1C_{2y} and C_1C_{2z} are the components of the vector $\overrightarrow{C_1C_2}$ and u_x, u_y and u_z are the components of unit vectors.

The system resolution with the Cramer method (Albarede, 1995) gives the variables k, k_1, k_2 and the ground point position A associated with each pair of homologous points according to the following equation:

$$\overrightarrow{OA} = \frac{\overrightarrow{OM_1'} + \overrightarrow{OM_2'}}{2} \Leftrightarrow \overrightarrow{OA} = \frac{\overrightarrow{OC_1} + \overrightarrow{OC_2}}{2} + \frac{k_1\overrightarrow{u_1} + k_2\overrightarrow{u_2}}{2} \tag{12}$$

References

Albarede, F., 1995. Introduction to Geochemical Modelling. Cambridge Univ. Press, Cambridge. 543 pp.

Baltsavias, E.P., 1995. Digital ortho-images—a powerful tool for the extraction of spatial- and geo-information. ISPRS J. Photogramm. Remote Sens. 51, 63–77.

Baratoux, D., Delacourt, C., Allemand, P., 1995. High Resolution Digital Elevation Models From Viking Images—new method and comparison with Mola data. J. Geophys. Res. 106 (E12), 32927–32942.

Blachut, T.J., Van Wijk, M.C., 1976. Results of the International Orthophoto Experiment 1972–76. PERS 42 (12), 1483–1498.

Ducher, G., 1991. Test on orthophoto and stereo-orthophoto accuracy. OEEPE Official Publication, vol. 25. Institute fuer Angewandte Geodaesie, Frankfurt. 227 pp.

Fabbri, O., Cappa, F., 2001. Apport de l'Analyse structurale à la compréhension de la dégradation du glissement de la Clapière, Massif du Mercantour, Alpes-Maritimes, EA 2642, Séance spécialisée de la SGF à Besançon, PNRN Risques Naturels.

Follaci, J.-P., 1987. Les mouvements du versant de la Clapière à Saint-Etienne-De-Tinée (Alpes-Maritimes). Bull. Liaison Lab. Ponts. Chaussees 150/151, 39–54.

Follaci, J.-P., 1999. Seize ans de surveillance du glissement de la Clapière (Alpes Maritimes). Bull. Liaison Lab. Ponts. Chaussees (Mars–Avril).

Follaci, J.-P., Guardia, P., Ivaldi, J.-P., 1988. Le glissement de La Clapière (Alpes Maritimes) dans son cadre géodynamique. Proc. 5e Symp. Int. Glissement Terrain, Lausanne.

Follaci, J.-P., Gastaud, J.-P., Durville, J.-L., 1989. Le point sur l'évolution dans le glissement de la Clapière (Alpes-Maritimes), BL 158, Inf 3371.

Fruneau, B., 1995. Interférommétrie différentielle d'images SAR-Application au glissement de terrain de La Clapière. Thèse de Doctorat, Paris 7.

Fruneau, B., Achache, J., 1995. Détection du glissement de terrain de Saint-Etienne de Tinée par Interférométrie SAR et modélisation. C.R. Acad. Sci., Paris 320 (IIa), 809–816.

Goepfert, W., 1984. Methods, accuracy requirements and applications of digital image rectifications. Proc. of 39th Photogrammetric Week. Institute of Photogrammetry, Univ. of Stuggart, 179–185.

Gunzburger, Y., 2001. Apports de l'analyse de la fracturation et de la modélisation Numérique à l'étude du versant instable de la Clapière (Saint-Etienne-De-Tinée, Alpes Maritimes). Mémoire de DEA PAE3S, ENSMN.

Gunzburger, Y., Laumonier, B., 2002. Origine tectonique du pli supportant le glissement de terrain de La Clapière (Nord-Ouest du massif de l'Argentera-Mercantour, Alpes du Sud, France) d'après l'analyse de la fracturation. C. R. Geosci. 334, 1–8.

Hobbie, D., 1974. Zur Verfahrendisposition bei differentieller Entzerrung von Photogrammetrishen Luftbildern. In DGK, Bayerishe Akademie der Wissenschaften, Reihe C., Dissertations, no. 197, Munich.

Jensen, J.-R., 2000. Remote sensing of the environment and the earth resource perspective. Prentice Hall Series in Geographic Information Sciences. Upper Saddle River, New Jersey. 530 pp.

Julian, M., Anthony, E., 1996. Aspects of landslide activity in the Mercantour Massif and the French Riviera, southeastern France. Geomorphology 15, 275–289.

Kasser, M., Egels, Y., 2002. Digital Photogrammetry. Taylor and Francis, London.

Kraus, K., Waldhäusl, P., 1994. 4th ed. Photogrammetry, Fundamentals and Standard Processes, vol. 1. Dummler, Bonn ISBN

3-427-78684-6. Translated in French by Grussenmeyer, P. and Reis, O.: Manuel de photogrammétrie—Principes et Procédés fondamentaux, Paris, Hermès editor. 407 pp., 1998.

Kraus, K., Otepka, G., Loitsch, J., Haitzmann, H., 1979. Digitally controlled production of orthophotos and stereo-orthophotos. PERS 45 (10), 1353–1362.

Malaroda, R., 1970. Carta geologica del Massiccio dell' Argentera, 1:50,000. Consiglio Nazionale Delle Ricerche.

Michel, R., Avouac, J.-P., 1999. Measuring ground displacements from SAR amplitude images: application to the Landers earthquake. Geophys. Res. Lett. 26 (7), 875–878.

Mikhail, E.M., Bethel, J.S., Mc Glone, J.C., 2001. Modern Photogrammetry. Wiley, New York. 479 pp.

Pothérat, P., 1994. Photo-interprétation du glissement de la Clapière–Analyse structurale cinématique du mouvement de 1955 à 1992. Proc. 7th International IAEG Congress, pp. 1527–1532.

Pothérat, P., Doridot, M., Chahine, M., 1999. L'utilisation de la photo-interprétation dans l'établissement des plans de prévention des risques liés aux mouvements de terrain. Laboratoire des Ponts et Chaussées, Paris Collection Environnement, p. 128.

Powers, P.S., Chiarle, M., Savge, W.Z., 1996. A digital photogrammetric method for measuring horizontal surficial movements on the Slumgullion earthflow, Hindsale county, Colorado. Comput. Geosci. 22 (6), 651–663.

Schaum, A., McHugh, M., 1991. Analytic method of image registration: displacement estimation and resampling. Technical report NRL Naval Research Laboratory, NDL report 9298, pp. 1–33.

Wolf, R.P., Dewitt, B.A., 2000. Element of Photogrammetry with Application in GIS, 3rd ed. McGraw-Hill, Columbus. 608 pp.